Quantification of ZnO Nanoparticle Uptake, Distribution, and Dissolution within Individual Human Macrophages

Simon A. James,[†,‡,⊗,*] Bryce N. Feltis,[§,⊥,⊗] Martin D. de Jonge,[†] Manoj Sridhar,[∥] Justin A. Kimpton,[†] Matteo Altissimo,[∥] Sheridan Mayo,[‡] Changxi Zheng,[#] Andrew Hastings,[§] Daryl L. Howard,[†] David J. Paterson,[†] Paul Frank A. Wright,[§] Gareth F. Moorhead,[‡,∥] Terence W. Turney,[⊥] and Jing Fu[▽,*]

[†]Australian Synchrotron, Clayton, Victoria 3168, Australia, [‡]Preventative Health Flagship (Materials Science and Engineering), CSIRO, Clayton, Victoria 3168, Australia, [§]School of Medical Sciences, RMIT University, Bundoora, Victoria 3083, Australia, [⊥]School of Chemistry, Monash University, Clayton, Victoria 3800, Australia, [∥]Melbourne Centre for Nanofabrication, Clayton, Victoria 3168, Australia, and [#]School of Physics and [▽]Department of Mechanical and Aerospace Engineering, Monash University, Clayton, Victoria 3800, Australia. [⊗]S.A. James and B.N. Feltis contributed equally.

ABSTRACT The usefulness of zinc oxide (ZnO) nanoparticles has led to their wide distribution in consumer products, despite only a limited understanding of how this nanomaterial behaves within biological systems. From a nanotoxicological viewpoint the interaction(s) of ZnO nanoparticles with cells of the immune system is of specific interest, as these nanostructures are readily phagocytosed. In this study, rapid scanning X-ray fluorescence microscopy was used to assay the number ZnO nanoparticles associated with ~1000 individual THP-1 monocyte-derived human macrophages. These data showed that nanoparticle-treated cells endured a 400% elevation in total Zn levels, 13-fold greater than the increase observed when incubated in the presence of an equitoxic concentration of $ZnCl_2$. Even after excluding the contribution of internalized nanoparticles, Zn levels in nanoparticle treated cells were raised ~200% above basal levels. As dissolution of ZnO nanoparticles is critical to their cytotoxic response, we utilized a strategy combining ion beam milling, X-ray fluorescence and scanning electron microscopy to directly probe the distribution and composition of ZnO nanoparticles throughout the cellular interior. This study demonstrated that correlative photon and ion beam imaging techniques can provide both high-resolution and statistically powerful information on the biology of metal oxide nanoparticles at the single-cell level. Our approach promises ready application to broader studies of phenomena at the interface of nanotechnology and biology.

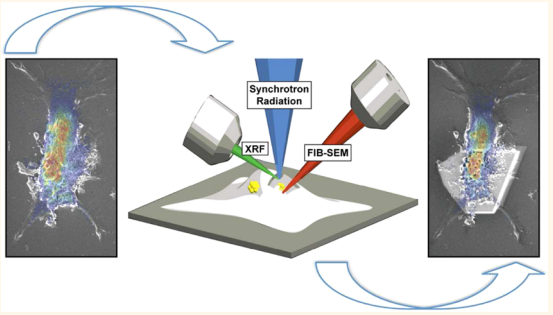

KEYWORDS: ZnO nanoparticles · X-ray fluorescence microscopy · cellular uptake · nanoparticle solubility · metallomics

Metal oxide nanoparticles (NPs) are now widely distributed in consumer products, despite only a limited understanding of how these objects interact with biological systems and the environment.[1−3] The inclusion of zinc oxide (ZnO) NPs in topically applied skin care products has resulted in increased public exposure to an inorganic nanomaterial directly linked to cellular dysfunction.[4−6] A recent study used ^{68}Zn-labeled ZnO NPs, which were synthesized *via* the same method employed in our current study, formulated in sunscreens applied to skin under "field conditions". This work demonstrated, contrary to the dominant view,[7,8] that a small amount of Zn (either as NPs or free ions) can penetrate healthy human skin and enter the bloodstream.[9] If intact NPs do reach living tissue, they are likely to elicit an immune response.[10] In particular, macrophages play a major role in safeguarding against assault by foreign bodies and are thus likely to experience relatively higher NP exposure than other cell types, a realization that has led to renewed interest in the interaction of ZnO NPs with cells of the immune system.[11] Agglomerates of ZnO NPs readily undergo phagocytosis and impair cell function,[12] alter cellular redox status,[13] and initiate apoptosis.[14] Dissolution of ZnO NPs, to liberate Zn^{2+},[15] is believed to precede these cytotoxic effects,[16] although ZnO NPs have been shown to have limited solubility in aqueous media.[17,18] However, recent observations of ionic zinc spontaneously forming

* Address correspondence to simon.james@synchrotron.org.au, jing.fu@monash.edu.

Received for review June 20, 2013 and accepted November 4, 2013.

Published online November 04, 2013
10.1021/nn403118u

amorphous carbonate/phosphate nanoparticulates in culture media,[19] coupled with the influence that individual particle topology, intracellular pH and the relative abundance of coordinating ligands can all exert on rates of particle dissolution, suggest a surprisingly rich solution chemistry for this nanomaterial once it enters the cellular environment. These effects conspire to make uptake, subcellular localization, and the mechanism(s) of toxicity difficult to elucidate.

Metal oxide NPs hold considerable promise as therapeutics and/or imaging agents in clinical settings, but to exploit their potential a more complete understanding of NP biology at the cellular level is required. In particular, research tools capable of identifying NPs in association with single cells and able to monitor changes in NP composition following endocytosis would provide valuable new understanding of their toxicology. However, such techniques must involve rapid and routine analysis while yielding sufficient statistical power. Current bulk analysis techniques like inductively coupled plasma mass spectrometry (ICP-MS) possess formidable minimum detection limits but are insensitive to intercell variation and require destruction of the sample.[20] Advances in laser ablation (LA-)ICP-MS have successfully extended this approach to provide quantitative spatially resolved information on elemental distribution, but currently such an approach cannot interrogate the nanoscale organization of elements within an intact cell.[21,22]

This has meant that investigations into the distribution of NPs (in either *in vitro* cell cultures or animal models) have typically been performed using transmission electron microscopy (TEM), oftentimes requiring the use of thin resin-embedded sections. However, TEM cannot be relied upon to conclusively identify NPs within a biological matrix due to particle aggregation, dissolution, contamination or morphological changes that occur upon cellular uptake.[23] Acquiring spatially resolved chemical information *via* electron energy loss spectroscopy (EELS) circumvents some of these issues and is highly valuable (EELS can be used to generate detailed 3-dimensional structural and chemical maps).[24] However, this approach has only been demonstrated on very thin specimens (typically <100 nm), and thus mechanical sectioning is necessary to render eukaryotic cells suitable for analysis despite the risk of compression artifacts distorting interpretation of recorded images.[25] Moreover, the hours of exposure to electron-beam irradiation required for chemical mapping can cause significant damage to biological specimens.[26] It is worth noting that advances in field emission SEM have allowed high resolution images of phagocytosed ZnO NPs to be acquired from intact cells,[27] but these techniques tend to be intricate and time-consuming if the study of many individual cells is required.

Both visible light and X-rays have found application for imaging inorganic species in biological systems. Cell permeable metal-specific optical fluorophores provide valuable information on pools of "exchangeable" ions,[28] but how these compounds interact with nanomaterials is less clear.[29] Moreover, when using these ligands, care must be taken to avoid spurious interpretations, stemming from NP dissolution, organelle-specific differences in ligand uptake, or local changes in pH or redox environment modifying the spectral characteristics of these fluorophores.[30,31] Recent work has highlighted the usefulness of X-ray imaging for tracking the distribution of NPs (including ZnO NPs) throughout mammalian cells, but this work has been limited to either cells loaded with chemically inert NPs containing high Z elements (providing high native contrast) or few individual cells.[15,31−34] Advances in the efficiency of X-ray fluorescence (XRF) detectors[35] have yielded alternative probes with which to interrogate the interactions of NPs with biological systems. Here we describe the use of rapid scanning X-ray fluorescence microscopy (XFM, for a recent review see ref 36) to determine the number of ZnO NPs associated with ∼1000 individual THP-1 monocyte-derived human macrophages and provide direct evidence that this cell type is able (at least partially) to dissolve ZnO NPs. Subsequently, and in concert with iterative rounds of focused ion-beam (FIB) ablation scanning electron microscopy (SEM), XFM was used to record quantitative information on NP distribution and dissolution postinternalization. These data provide direct *in situ* evidence for cell-mediated breakdown of ZnO NPs occurring within the cellular interior.

RESULTS AND DISCUSSION

Particle Characterization and Sample Preparation. Dissociation of ZnO NPs inside cells is believed to be critical to their biological impact[4,15,16,37] but is difficult to observe *in situ*, because of the confounding presence of physiological Zn. To overcome this hurdle, we have developed an approach utilizing ZnO NPs doped with a small amount of Co^{2+}.[38] Crucially, inclusion of Co has no influence on the cytotoxicity of these structures relative to the undoped form of the material (Figure S1A, Supporting Information). The Co-dopant allowed the distribution of ZnO NPs to be tracked through biological media without any need for modifying the particle's surface by attaching optically fluorescent tags that may alter cellular uptake and processing.

Characterization of the Co-doped and undoped ZnO NPs has been described elsewhere;[38] both materials were made available through Micronisers (Victoria, Australia) using their commercial processes. Briefly, X-ray powder diffraction (XRD) of Co-doped and undoped ZnO NPs exhibited the characteristic wurtzite structure. Rietveld refinement was used to calculate the *c*-axis lattice parameter; c = 5.2150(2) Å and c = 5.208(2) Å, respectively, values almost identical to the standard diffraction data observed for bulk ZnO (ICDD card number 36−1451, c = 5.206 Å) and consistent with

TABLE 1. Characterization of (Co,Zn)O and ZnO NPs Agglomeration under Different Conditions[a]

	nanoparticle type			
	ZnO NPs		(Co,Zn)O NPs	
	mean size (nm)	1σ (nm)	mean size (nm)	1σ (nm)
TEM	25	7	30	8
XRD	57	9	48	6
DLS (D_{90})[b,c]	40	6	39	5
DC[d]	1330	300	1390	340

[a] Various analytical techniques (TEM, transmission electron microscopy; XRD, X-ray powder diffraction; DLS, dynamic light scatter; DC, disc centrifuge) were used to compare the size distribution and agglomeration of the two ZnO nanoparticles used in this study. [b] Assuming nominally spherical particles and a density of 5.61 g cm^{-2}, we estimated the surface area of the primary Co-doped nanoparticles to be ~30 m^2 g^{-1}. [c] Measurement performed on nanoparticles suspended in water. [d] Measurement performed on nanoparticles suspended in RPMI-1640 media, containing 5% (v/v) fetal bovine serum.

previous reports (Figure S1B, Supporting Information).[39] The same analysis indicated that the average crystallite size for doped and undoped ZnO NPs was similar (Table 1), minimizing the likelihood that differential strain effects will influence particle stability. The mass of Co incorporated into NPs used in this study was assessed to be 1.8% (w/w), *via* ICP-MS, corresponding to a Zn:Co molar ratio of 39:1. These data are consistent with previous work demonstrating that Co substitutes isomorphously for Zn into the ZnO sublattice with uniform incorporation of the dopant at up to 3% (w/w).[38−40]

The morphology of Co-doped and undoped ZnO NPs was very similar, as observed under TEM (inset, Figure S1B, Supporting Information). Estimates of the primary particle size and dispersion were performed on particulates suspended in water using dynamic light scattering (DLS). The DLS and TEM measurements were consistent, as the DLS showed Co-doped and undoped NPs to be comparably sized objects, with D_{90} values of 39 ± 5 and 40 ± 6 nm, respectively (Figure S1C, Supporting Information). The influence of biological molecules (particularly proteins) on particle dispersion is nontrivial,[41] and attempts to measure the primary particle size using culture media as the suspension solvent gave ambiguous results, suggesting low quality dispersion. This behavior was likely due to the complex (and not well understood) interaction(s) between NPs and the various components present in RPMI media,[42] compounded by the presence of fetal bovine serum (FBS).[43] Disk centrifugation has advantages when sizing particulates under these challenging conditions,[44] and was used to establish the size distribution and agglomeration of particles suspended in physiologically relevant fluids. This analysis showed typical agglomerate sizes of ~1.4 μm for both Co-doped and undoped NPs. A summary of particle characterization is presented in Table 1.

Finally, the stability of Co-doped and undoped ZnO NPs was tested under a variety of physiological conditions. By monitoring the amount of Zn that had dissociated from preparations of intact NPs after a 24 h incubation under relevant conditions, we saw that incorporation of Co had little effect on the stability of ZnO NPs; data are presented in Table 2.

For *in vitro* exposures, THP-1 monocyte-derived human macrophages were incubated for 24 h with or without 20 mg L^{-1} of (Co,Zn)O NPs, 20 mg L^{-1} of ZnO NPs or 15 mg L^{-1} of $ZnCl_2$; each concentration was selected to induce equivalent cytotoxicity (Figure S1A, Supporting Information). Although performing elemental analysis on hydrated specimens is possible,[16,45] multiple rounds of XFM and EM imaging were anticipated to be required for this study. Thus, to improve stability, specimens were extensively washed with fresh media after incubation with NPs and before being chemically fixed (with glutaraldehyde and osmium tetroxide) and dehydrated. Our choice of fixative was driven by a desire to preserve the integrity of the plasma membrane[46,47] and to capture the entire system (both cells and growth substrate) with minimal interference or disruption of cell topology. Washing with low pH buffers was avoided so that the chemical composition of extracellular NP agglomerates could be investigated as part of the study.

Indentifying ZnO Nanoparticles *in Situ*. XFM has demonstrated utility for studying bioinorganic chemistry *in situ*,[35] and recent reports have employed this technique for studying biological interactions of ZnO NPs.[15,27,48] A representative integrated XRF spectrum acquired from a single NP-treated macrophage confirmed that this approach was able to identify the major elemental constituents of our specimen type (Figure S1D, Supporting Information). These data were used to construct high resolution elemental maps of THP-1 macrophages, either untreated or treated with (Co,Zn)O NPs (Figure 1A). As expected, endogenous cobalt levels (*i.e.*, Co associated with non-NP treated macrophages) were below experimental detection limits and is consistent with the low abundance of Co in biological systems.[49] These data confirmed that Co could be used as a sensitive marker for tracking NP distribution and provides useful dual-label confirmation of the presence of intact Co-doped ZnO NPs within cells.

A caveat with this approach is the sensitivity of XFM to the presence of elements through the full thickness of a specimen. This makes the discrimination between NPs interacting with a cell, and those particulates that have simply precipitated out of solution and settled upon the cell's exterior, problematic. Even though ZnO NPs are reported to be readily internalized,[15,27] we sought to assess the degree to which treated cells became surface-decorated with NPs. If precipitation on the cell surface drives cellular accumulation of NPs, then larger cells (having greater projected area) should

TABLE 2. Characterization of (Co Zn)O and ZnO NP Stability under a Range of Physiological Conditions

	nanoparticle type					
	ZnO NPs			(Co,Zn)O NPs		
	concentration (mM)	1σ (mM)	% Zn dissolved[a]	concentration (mM)	1σ (mM)	% Zn dissolved[a]
water	0.028	0.002	2.20 $\pm$ 0.1	0.024	0.001	1.8 $\pm$ 0.1
RPMI-1640 + FBS	0.012	0.001	0.93 $\pm$ 0.1	0.013	0.001	1.0 $\pm$ 0.1
ALF	1.256	0.016	98.0 $\pm$ 0.1	1.214	0.010	95 $\pm$ 0.7

[a] The concentration of Zn that entered solution after 24 h incubation in water, cell culture media (RPMI media containing 5% (v/v) foetal bovine serum) or artificial lysosomal fluid (ALF), was assessed *via* ICP-MS. The third column shows this value as a percentage of the original molarity of Zn (1.28 mM in both cases).

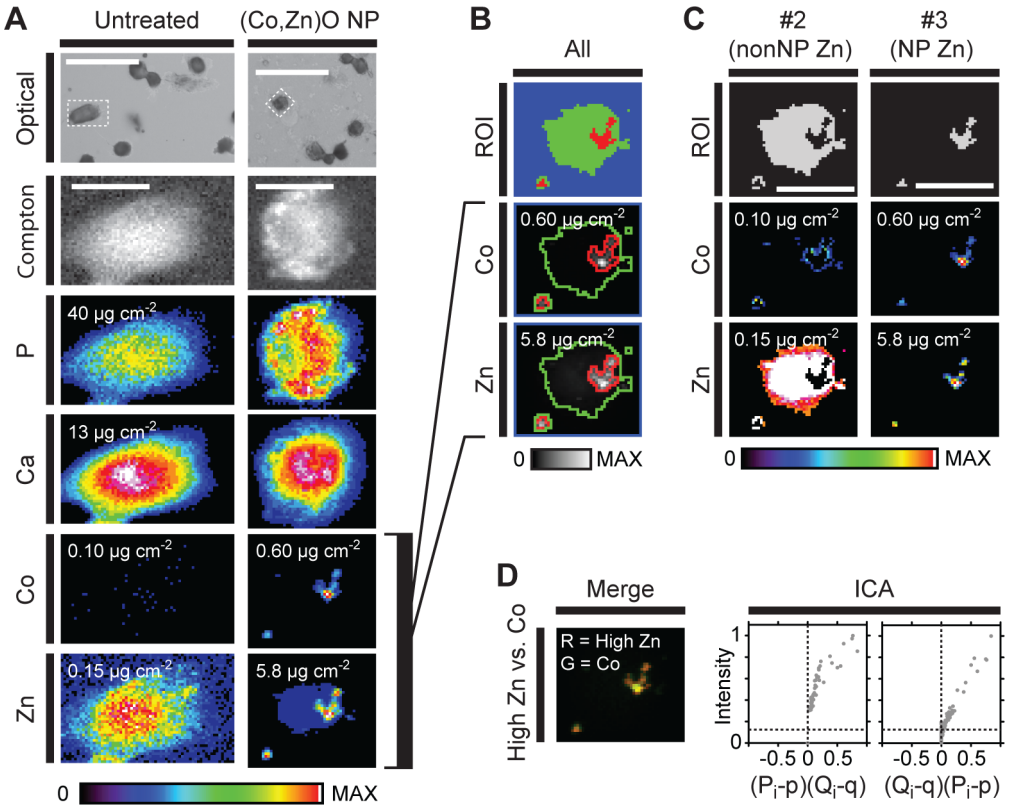

Figure 1. Identification of agglomerated NPs in association with THP-1 macrophages. (A) Optical micrograph of THP-1 macrophages, untreated and treated with (Co,Zn)O NPs (scale bar 45 μm). The dashed-line white box indicates a cell from each treatment group selected for high-resolution elemental mapping. Inelastic scatter (Compton) of incident photons was used to demarcate the boundary of the cell under investigation (scale bar 10 μm). The color scheme for each element is scaled separately, with the maximum pixel value shown numerically at the top left of the relevant panel. (B) Segmentation of the Zn map recorded from the NP-treated cell identified in A, using *k*-means cluster analysis. The three distinct ROIs (blue = ROI#1, green = ROI#2 and red = ROI#3) correspond to collections of pixels consistent with a unique mean concentration of Zn. The Co and Zn maps from A are reproduced (in gray scale) with the boundaries of each ROI superimposed. Maximum pixel values are shown numerically at the top left of the relevant panel. (C) Binary masks corresponding to ROI#2 and ROI#3 (identified in B as green and red, respectively) were applied to the Co and Zn maps recorded for the NP-treated cell presented in A. The color scheme for each element is scaled equivalently to that used for corresponding elemental maps of the untreated cell presented in A; maximum pixel values are shown numerically at the top left of the relevant panel. (D) Intensity correlation analysis (ICA) was used to test the degree of covariance between the elevated Zn and Co present within ROI#3 (defined in B). These plots show normalized pixel intensity (*y*-axis) for each component (*P*/*p* = Zn and *Q*/*q* = Co) against the $(A_i - a)(B_i - b)$ function (*x*-axis). The calculated Li's intensity correlation quotient (a global estimation of colocalization) was $\geq$0.41, indicating the pixel intensities were strongly covarying; hence, elevated Zn is strongly correlated with Co within ROI#3.

be associated with a greater number of NPs. By correlating a cell's projected area with the mass of cellular Co, we found that cell size accounted for only 8% of the variation in Co load (1007 cells; $r = 0.29$, $p < 0.0001$). This finding is inconsistent with NPs being passively accreted on cell surfaces after simply settling out solution and thus confirmed that treated cells accumulate NPs through active processes.

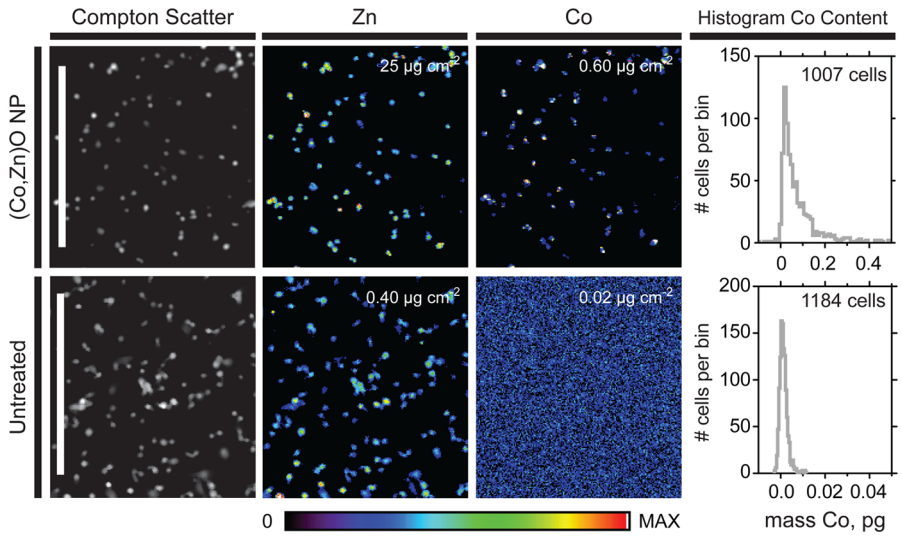

Figure 2. Quantitating cellular Co load in a population of THP-1 macrophages. High definition elemental maps of a representative area (~12% of total scan area) showing THP-1 macrophages either untreated or treated with 20 mg L^{-1} (Co,Zn)O NPs (scale bar 300 μm). Again inelastic scatter (Compton) of incident photons was a useful guide to identify cell boundaries. The color scheme for each element is scaled separately, with the maximum pixel value shown numerically at the top right of the relevant panel. Accompanying these images are histograms (tabulated frequency) of cellular Co content along with the number of cells included in the analysis. Cells not exposed to NPs had little endogenous Co, and the observed low intensity, spatially uniform Co XRF was dominated by experimental background. The average Co signal associated with untreated cells was used to calculate the minimum number of (Co,Zn)O NPs detectable within a single pixel to be $2.8 \pm 0.2 \times 10^2$ particles.

The active accumulation of exogenously applied (Co,Zn)O NPs indicated that Co XRF in cells should be associated with elevated Zn levels. Using *k*-means cluster analysis, the Zn map of treated cells could be segmented into three distinct regions of interest (ROIs), each associated with a unique mean Zn concentration (Figure 1B). Zn levels within ROI#3 spiked orders of magnitude above basal levels (untreated cells) or the Zn levels present in ROI#1 and ROI#2, and is consistent with the material in ROI#3 being agglomerated NPs. If true, we expected a high degree of colocalization between the Zn present in ROI#3 and the distribution of Co throughout the cell. Colocalization between Zn and Co within ROI#3 was assessed using intensity correlation analysis (ICA, Figure 1C),[50] for which Li's intensity correlation quotient (ICQ) was 0.41, implying excellent coregistration of these two signals. These data provided confidence that the distribution of Co could be used to identify subcellular regions that are biologically equivalent to ROI#3. In effect the map of Co distribution could be reliably employed for tracking the location of agglomerated NP material *in situ*.

Quantifying Cellular Accumulation of ZnO NPs. In addition to the Co label, facilitating the tracking of NPs in the culture media system, it also provided a means to quantify the number of NPs in association with a single cell. Based on the ICP-MS and DLS analysis detailed above, a single (Co,Zn)O NP could be expected to contain $\sim 3.4 \times 10^{-18}$ g of Co. The mass of Co associated with a single cell (as measured by XFM) enabled the cell's Co load to be converted into the equivalent number of NPs, a value henceforth referred to as the cellular NP-load. Traditionally, XFM experiments are time-consuming, making such an approach for assessing NP-loading across a large number of cells impractical. However, because of advances in low-latency XRF detectors (such as the Maia installed at the Australian Synchrotron),[51] rapid, high-definition XFM (with elemental maps containing ≥100 000 pixels) is becoming more routine.[34,52] Taking advantage of improved data acquisition rates enabled high-definition elemental mapping of approximately 1000 individual NP-treated THP-1 macrophages to be completed in under an hour. Using these data to quantify the mass of Co associated with each cell then formed a basis with which to measure the NP-load per cell (Figure 2 and Figure S2, Supporting Information).

Perhaps surprisingly, the resulting histogram of cellular NP-load was not normally distributed around a single mean, but rather these data were distributed log-normally (Figure 3A). This distribution commonly describes the abundances of molecules within cellular systems,[16,53,54] even the accumulation of platelets within THP-1 macrophages *via* phagocytosis has been shown to be log-normal.[55] In this case the result was rationalized by appealing to the probability of a single platelet being internalized as the product of multiple independent events (consistent with the multiplicative version of the central limit theorem).[56] Interestingly, as endocytosis is ultimately driven by a number of gene products, another biological interpretation of these data is that some determinant of gene expression capacity (*e.g.*, availability of mRNA, access to promoter(s), sufficient number of ribosomes, stage of cell cycle, *etc.*), if normally distributed among different cells, could lead to a log-normal distribution of

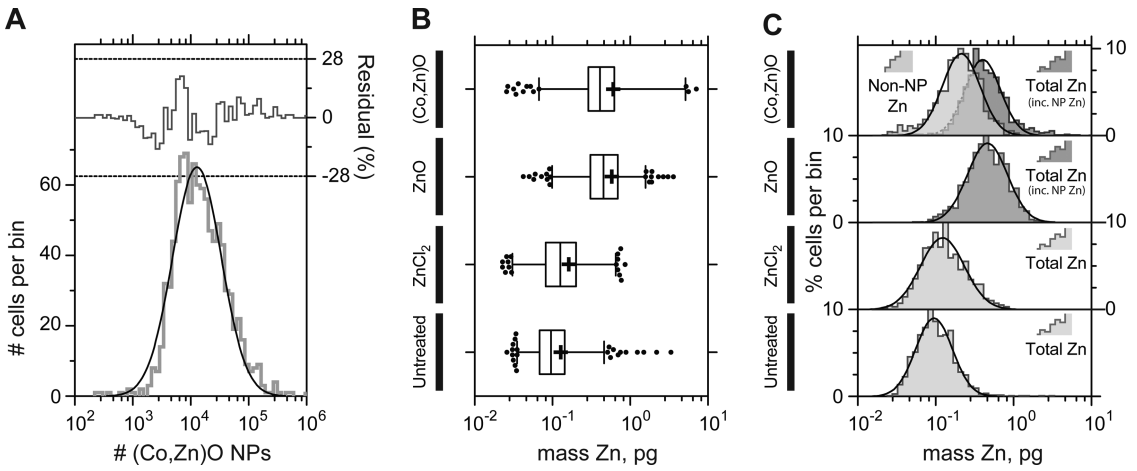

Figure 3. Quantifying NP-load, a population study. (A) The histogram (tabulated frequency) of NP-load for THP-1 macrophages treated with (Co,Zn)O NPs was well modeled by a single log-Gaussian curve (solid black line). (B) Box and whisker plot displaying mass of Zn associated with cells from THP-1 macrophages either untreated, treated with $ZnCl_2$, ZnO NPs, or (Co,Zn)O NPs. The box includes the 2nd and 3rd quartiles, and the whiskers encompass 1−99% of the data range; outliers are shown as single solid black circles (●); means and medians are indicated by (+) and (|), respectively. Data are presented on a logarithmic *x*-axis. As cellular Zn load was not normally distributed, the log-transformed data for each group was compared using a one-way ANOVA, and significant elevations (above basal, $p < 0.001$) in mean cellular Zn were observed for cells exposed to either Co-doped or undoped ZnO NPs and $ZnCl_2$ (with Bonferroni's multiple comparison *posthoc* test). (C) Histograms (tabulated frequency) of cellular Zn content for each treatment group. For the cells treated with (Co,Zn)O NPs, both non-NP Zn (light gray) and total Zn (non-NP + NP Zn, dark gray) are shown separately; for the other treatments, only data for total Zn are shown. In all cases these data were well modeled by single log-Gaussian curves (solid black line), and the log-mean from each treatment group was compared using one-way ANOVA (with Bonferroni's multiple comparison *posthoc* test) with significant elevations (above basal, $p < 0.001$) of non-NP Zn and/or total Zn (as appropriate) observed for cells treated with (Co,Zn)O NPs, ZnO NPs, and $ZnCl_2$.

NP-load.[57] Though we lack a specific model to explain our current observations, these initial findings suggest that using XFM to follow the fate of mixed metal oxide NPs may prove a fruitful approach with which to disentangle these effects in future studies.

Importantly, these data imply that care must be taken when analyzing population data on cellular NP-load. For example, simply reporting the arithmetic mean without accounting for the observed deviation from normality (by logarithmically transforming the data) will distort interpretation (Figure 3B).[53] Consequently, we first log-transformed the data and assessed whether it was normally distributed before calculating the mean and variance of NP-load for the treated population ($n = 1007$). This log-mean NP-load was back-transformed for presentation, giving a value of 1.5×10^4 particles (-1σ to 1σ: 0.5 to 4.1×10^4 NPs).

Effect of NP Treatment on Cellular Zn Load. Relative to untreated cells, THP-1 macrophages exposed to ionic Zn (applied as $ZnCl_2$) showed minimal increase in total cellular Zn load (1.3 fold) compared to cells treated with either Co-doped or undoped ZnO NPs (4.4-fold and 4.6-fold respectively, Figure 3B). Interestingly, these treatments induced equal cytotoxicity despite NP-treated cells being exposed to 30% more exogenous Zn. These data provided strong evidence that Zn^{2+}, which readily forms stable complexes with endogenous ligands (as per the Irving−Williams series),[58] is a more potent disruptor of cell function than the relatively inaccessible Zn sequestered within crystalline ZnO NPs. This reasoning implicated NP dissolution as being central to the observed cytotoxicity[16,59,60] and is consistent with previous work undertaken in other cell lines.[15]

The inclusion of the Co-dopant in ZnO NPs enabled us to test this hypothesis directly. Excluding subcellular regions where the presence of (Co,Zn)O NPs dominated the contribution to Zn XRF (defined by the presence of Co), we observed a 2-fold increase (beyond basal levels) in non-NP Zn for the (Co,Zn)O NP-treated cells. These data show that leakage of Zn from the agglomerated (Co,Zn)O NP material into the cellular interior elevated the Zn levels only marginally higher than the increase induced by equitoxic treatment with $ZnCl_2$ (Figure 3C). This result suggests that treatment with ZnO NPs or Zn^{2+} causes cytotoxicity through similar mechanisms, namely by overwhelming the cell's capacity to appropriately buffer intracellular Zn levels.[61] This interpretation is supported by previous work relating increased particle stability with an improved cytotoxicity profile.[6,37,61]

Because of the specimen preparation procedure (involving extensive washing prior to analysis), we were unable to account for the totality of exogenously applied Zn, which prevented a definitive assessment of the proportion of total ZnO NPs dose that was internalized by cells over the course of the exposure period.

Cell-Mediated Dissolution of (Co,Zn)O NPs. The quantification of cellular NP-load (Figure 3A) implied that for a NP-treated macrophage associated with a typical

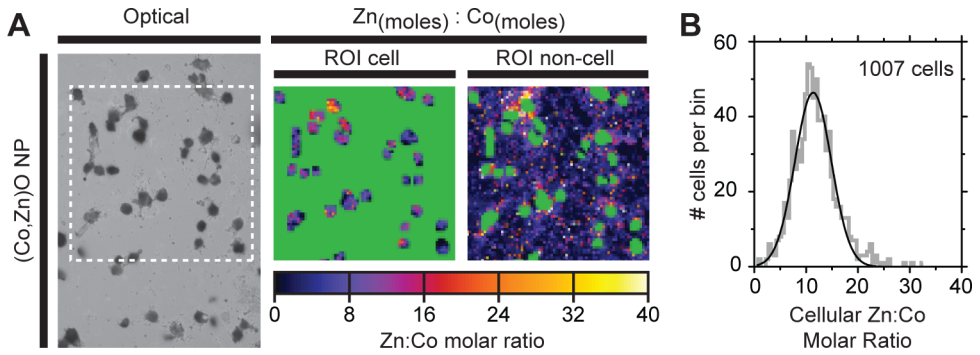

Figure 4. Cell-mediated dissolution of (Co,Zn)O NPs. (A) Optical micrograph showing a representative field of THP-1 macrophages treated with (Co,Zn)O NPs. The next two panels show the ratio of Zn:Co (in moles) for the representative area within the dashed-line white box shown in the first panel. The color scheme for both panels reflect the molar ratio of Zn:Co in arbitrary units. To aid the reader the image has been separated into "cell" and "noncell" regions (panels as indicated) to highlight the extracellular location of intact NP deposits (Zn:Co molar ratio = 39:1). Green regions within these two panels have been masked out for display. (B) Histogram (the tabulated frequency) of the Zn:Co molar ratio for NP agglomerates associated with macrophages. These data were well modeled by a single Gaussian curve (solid black line) centered at 11 (-1σ to 1σ: 7.8 to 15); the spread of these data suggest the agglomerated material is present in differing states of dissolution.

number of (Co,Zn)O NPs (1.5×10^4 particles), the total mass of cellular Zn should be elevated ~80-fold beyond basal levels (basal total Zn load being 0.10 pg, -1σ to 1σ: 0.06 to 0.17 pg, Figure 3B). It was surprising then that total Zn levels observed in these cells (treated with either Co-doped or undoped ZnO NPs) increased only ~4-fold (Figure 3B,C). This discrepancy between NP-load (calculated using cellular Co content) and total cellular Zn levels indicated that particle dissolution was occurring.

Freshly prepared, intact (Co,Zn)O NPs had a Zn:Co molar ratio of 39:1; therefore, we could monitor changes in this ratio for cells treated with Co-doped ZnO NPs and characterize this particle dissolution *in situ*. Our initial characterization of particle stability indicated that, within the exposure period (24 h), minimal particle dissolution had occurred around neutral pH (Table 2). In addition, when (Co,Zn)O NPs were incubated (24 h) under various abiotic conditions, only small changes to particle composition were observed (Figure S3, Supporting Information). In contrast, we were unable to identify any cell-associated NP agglomerates with Zn:Co molar ratio greater than 35 (Figure 4A). Indeed, the mean Zn:Co molar ratio was markedly lower at 11:1 (Figure 4B), representing a significant enrichment of Co (relative to Zn) when compared to fresh preparations of intact NPs (Figure S3, Supporting Information). Importantly, we were also able to identify significant deposits of intact extracellular NP agglomerates, where the expected Zn:Co molar ratio of 39:1 was maintained (Figure 4A).

Although NPs incubated (24 h) in abiotic media and subsequently fixed (Figure S3, Supporting Information) did show a small enrichment of Co (1.1-fold) that was consistent with limited particle dissolution, this minimal effect was unable to account for the large change in NP composition observed when this same material was incubated in the presence of THP-1 macrophages (3.5-fold). These data provide compelling evidence that particle dissolution is dependent on biological processes and not simply a consequence of the extended incubation.

Identifying intact undoped ZnO material within cells remains challenging, making it difficult to compare whether particle dissolution is occurring to the same extent as in cells treated with (Co,Zn)O NPs. However, given that Co-doping had little effect on particle morphology, stability, or cytotoxicity (Tables 1 and 2, Figure S1, Supporting Information), and that both NP-treatments elicited similar elevations in total cellular Zn load (Figure 3B,C), it appears from the Co-doped ZnO analyses that cell-mediated dissolution of ZnO (with concomitant elevation in non-NP Zn) drives cellular dysfunction (at least to first order). What role(s) the small amount of Co present in the doped material may play in these processes is difficult to say. We have not seen evidence in this study that Co-doping, either when sequestered within intact NPs or when freed upon particle dissolution, influences the particle stability, NP uptake, metabolism or cytotoxicity (Tables 1 and 2, Figures S1 and S3, Supporting Information, and Figure 3). While we are confident that the elevation in non-NP Zn is a major factor leading to cytotoxicity (Figure 3C), the presence of Co may still have secondary effects on cell function that were below the level of detection for our suite of assays.

Leakage of Zn from Agglomerated NPs. While the population studies presented above are powerful and illustrative they do not address the details of NP uptake or localization. Thus in an effort to further elucidate the mechanisms underlying ZnO NP-induced cytotoxicity, representative (Co,Zn)O NP-treated and Zn^{2+}-treated cells were selected for high resolution elemental mapping (Figure 5). Consistent with previous results the molar ratio of Zn:Co within the NP agglomerates of the NP-treated cell shown in Figure 5 was 11:1. Using

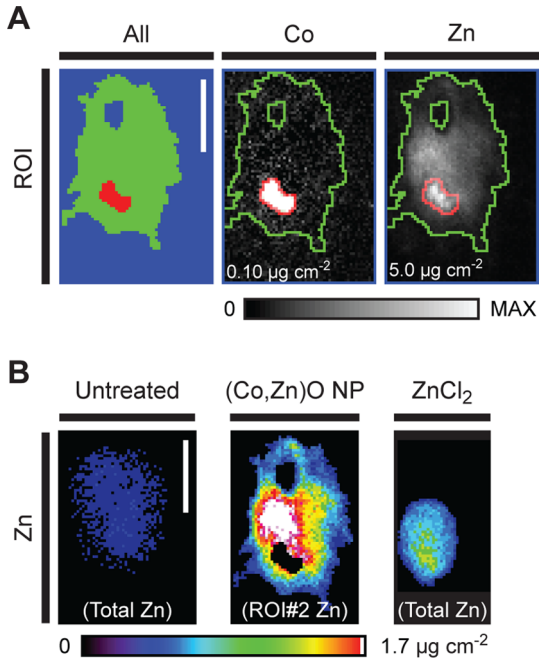

Figure 5. Leakage of Zn from (Co,Zn)O NPs dissolution elevates cellular Zn levels. (A) *k*-Means cluster analysis (as used in Figure 1) was used to segment the high-resolution Zn map recorded from a NP-treated cell (ROIs: blue = ROI#1, green = ROI#2, and red = ROI#3, scale bar 8 μm). The distribution of Co and Zn are shown (in gray scale) with the boundaries of each ROI superimposed, as presented in Figure 1B. The color scheme for each element is scaled separately with maximum pixel values shown numerically at the bottom left of the relevant panel. (B) High-resolution elemental map of Zn distribution within ROI#2 of the (Co, Zn)O NP-treated cell presented in A. For comparison representative high resolution Zn maps (total Zn) for an untreated and $ZnCl_2$-treated cell are shown alongside. All three images are presented on a uniform color scale (maximum pixel value as indicated, scale bar 8 μm).

k-means cluster analysis, the Zn map for (Co,Zn)O NP treated cells was segmented into three ROIs (as described above), and as before ROI#3 contained greatly elevated levels of both Zn and Co (Li's ICQ of 0.47, Figure 5A). As expected ROI#2 had a significantly lower areal density of Zn than ROI#3 but still 8-fold higher than Zn levels in the untreated cell (Figure 5B). Unlike Zn however, there was little evidence for Co entering the cellular interior, as despite ROI#3 being much smaller than ROI#2, almost the entire cellular Co content (>97%) was contained within ROI#3.

These data implied that even after partial dissolution, cell-associated NPs remained somewhat intact (despite selective loss of Zn); it is less likely that after complete particle dissolution, the Zn and Co remained within the same intracellular structures but with preferential loss/export of Zn. In either case these results confirmed dissolution of NPs allowed the liberated Zn to leak into the surrounding cytoplasm (Figure 5B). The different solution chemistries of Zn^{2+} and Co^{2+}, coupled to the complex and poorly understood details of endocytic metal transport,[62−64] suggest that further work is needed to understand the mechanism(s) behind this observation. However, given the relatively simple quantitative relationship between elemental content and XRF, this approach of monitoring the exchange of metals (or metal oxide NPs) between subcellular compartments could be useful for studying phagosomal metal homeostasis.[65,66]

The interaction between cells and zinc is highly complex.[67] The currently accepted paradigm for ZnO NP cytotoxicity follows several phases of action; NPs are taken into the cell, NPs then destabilize releasing zinc ions, and finally these zinc ions perturb the cell's antioxidant defenses, leading to oxidative stress, cellular damage and eventual cytotoxicity. The inherent complexity and scale of these mechanisms has meant that there is no single study in the literature exploring the entire ZnO NP mode of action. However, a significant amount of detail can be elucidated from numerous smaller studies, even though not all are in complete agreement.

One of the most significant factors for understanding the mode of action is the point at which ZnO NPs dissolution occurs. Some previous work has suggested that ZnO NPs dissolved extracellularly,[4] and while NP solubility can vary significantly, it is generally accepted that ZnO NPs are more unstable outside a neutral pH.[68] Such instability at low pH increases the likelihood of intracellular dissolution during cellular uptake and processing, as endosomal pH is reduced. That is, pH progressively decreases from the early endosome (pH 6.3) to the late endosome (pH 5.5) stage, while for phagocytic cells, the lysosome is even more acidic (pH is 4.7).[69] The relative insolubility of ZnO NPs at neutral pH might explain why some reports have shown contact between cells and NPs to be an absolute requirement for cytotoxicity,[17] including our own work on the solubility of ZnO NP in cell culture media.[19] There are numerous studies using ZnO NPs that show some relationship between zinc release and cytotoxicity.[37,59,60] Of these, Xia and co-workers showed that NP dissolution could be reduced with iron doping, which in turn decreased their cytotoxicity. To add extra complexity, it has also been reported that ZnO NPs can cause lysosome destabilization,[70] and that free zinc can induce Zn^{2+}-dependent protein activity disequilibrium,[71] both of which could also reduce cell viability. It must be noted that all of these studies have only shown correlations between intracellular zinc and cytotoxicity, meaning that direct causality can still only be inferred.

An additional mechanistic component in the ZnO NP-dependent cytotoxicity pathway is the generation of reactive oxygen species (ROS). Paralleling the investigation of intracellular zinc levels, ROS has also been implicated in the cytotoxicity of ZnO NPs,[3] with ZnO NPs also elevating levels of ROS in mammalian cells.[16,72,73] An important consideration is that zinc released from ZnO NPs cannot directly catalyze ROS generation, as it is not a redox-cycling transition metal. However, high intracellular zinc concentrations can

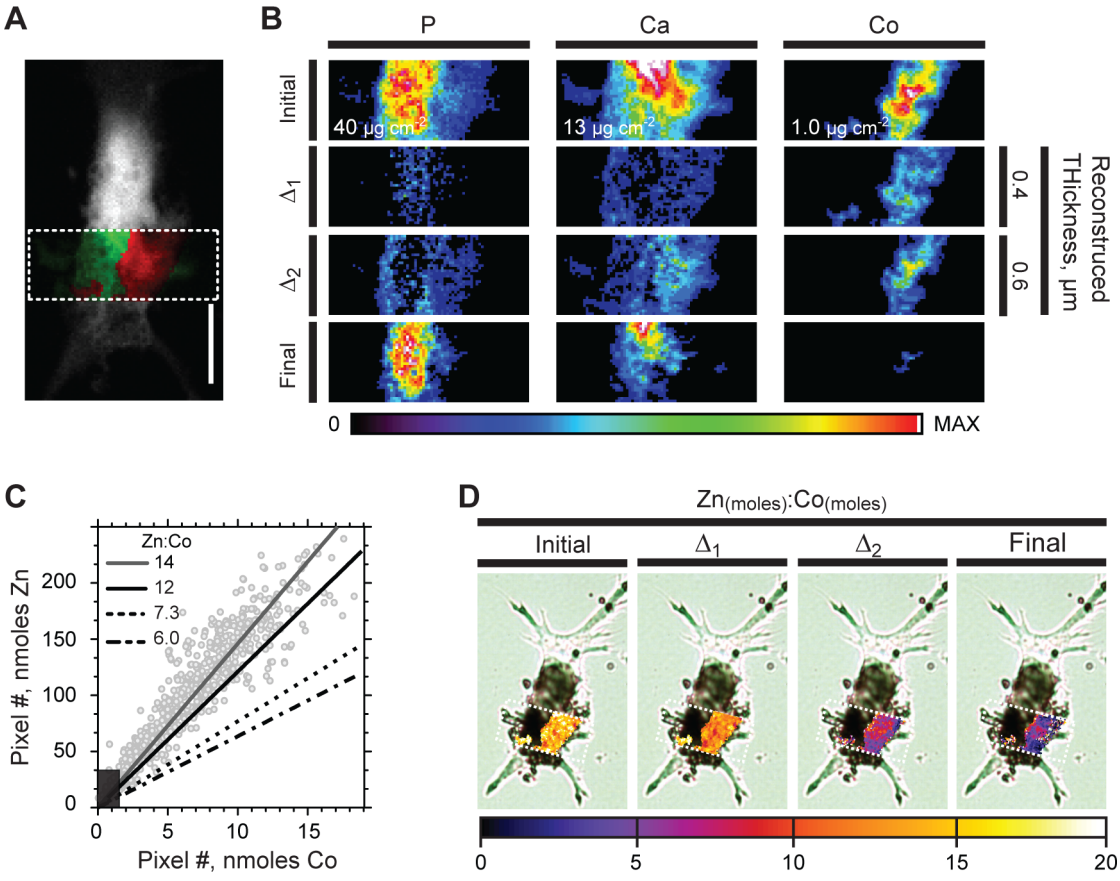

Figure 6. Investigating intracellular (Co,Zn)O NP uptake and distribution. (A) High resolution Zn map (scale bar 10 μm) of the targeted cell; the region selected for 5 cycles of iterative XFM FIB-SEM is contained within the dashed-line white box. Red and green demarcate regions where Zn is present as part of agglomerated NPs (red) from the non-NP containing region (green). (B) High resolution elemental maps of the region identified in A, before (initial) and after (final) the 5 ablation cycles. By recording XFM maps before and after each ablation cycle, the distribution of elemental content within the ablated material could be reconstructed for selected intracellular volumes (reconstructed layers are designated, Δ_n), thickness of the reconstructed layer as indicated. The color scheme for each element is scaled separately, and maximum pixel values are shown numerically at the bottom left of the relevant panel. (C) For each set of elemental maps shown in B, a scatter plot displaying the relationship between Zn and Co at each pixel within the NP-agglomerate identified in A. Linear regression of these data revealed the Zn:Co molar ratio within the NP-agglomerate changed as a function of internalization depth (720 pixels, r; initial (preablation) = 0.96 (solid gray line), Δ_1 = 0.94 (solid black line), Δ_2 = 0.96 (dotted black line), final (postablation) = 0.97 (dashed black line), $p < 0.001$). Data with values less than 15% of the maximum were excluded from the analysis (dark box). For clarity only data from the initial (preablated) scan are shown (gray circles). (D) Map of the Zn:Co molar ratio within each reconstructed layer (shown in B) superimposed over an optical micrograph of the target cell. This representation highlights the change in NP composition as a function of internalization depth. Color scheme reflects the Zn:Co molar ratio, and each reconstructed layer is presented on a uniform color scale.

indirectly induce ROS by competing out other reactive transition metal ions from their binding sites in oxidative stress defense macromolecules, such as metallothionein, and these Fe and Cu ions are then available to catalyze Fenton-type reactions.[74,75] Excessive zinc levels can also damage organelles, such as mitochondria, resulting in electron leakage to oxygen and elevating intracellular superoxide.[76] Our recent work directly demonstrates a very strong correlation between intracellular zinc, ROS generation, and cytotoxicity after ZnO NP exposure in human THP-1 immune cells.[77]

Quantitation of Internalized NP Load. As eluded to above, the penetrating nature of X-rays meant that the preceding experiments could not unambiguously differentiate between internalized NPs or those resting in close proximity to the plasma membrane. Data presented in Figures 1−5 are consistent with (Co,Zn)O NPs being (i) present throughout the volume of the cell; (ii) attached to the exterior of the plasma membrane without internalization; or (iii) a combination of these scenarios. To address this issue a novel strategy combining XFM and FIB-SEM (outlined in Figure S4, Supporting Information) was developed and employed to evaluate the proportion of cell-associated (Co,Zn)O NPs that were actually internalized. To this end we selected a single macrophage (cellular NP-load, $3.2 \pm 0.4 \times 10^4$ NPs) for further detailed analysis (Figure S5, Supporting Information), and a series of controlled doses of Ga^+ ions were used to ablate material from the cell surface. The efficiency of the ablation process had been previously characterized on parallel specimens *via* AFM (Figure S6, Supporting Information), and the dislocation of

Zn or Co during the FIB process was expected to be negligible (Figure S7, Supporting Information).

Elemental maps recorded pre- and postablation of the first 100 nm thick layer of material closest to the cell surface showed a reduction in elemental XRF from the milled region, observations that matched with a congruent reduction in cellular material observed *via* SEM (Figure S8, Supporting Information). This amounted to a significant reduction in "NP Zn" postablation and indicated that ~50% of the cells NP-load; some $1.7 \pm 0.3 \times 10^4$ NPs were partitioned at the plasma membrane/within early endosomes.

Characterization of Internalized NPs. Recent studies of ZnO NP internalization using ultrathin sections of mouse macrophage J774.1 cells indicated that after 3 h a small amount of electron dense material, likely NPs, had invaded the cellular interior, but that these structures were no longer detectable after 24 h.[27] Although the current study used significantly larger ZnO NPs (40 nm compared to 5−10 nm)[27] and a human cell line, we sought to assess the extent to which NPs had penetrated into the cell. The subcellular distribution of internalized NPs were assessed using iterative XFM FIB-SEM; in each case a defined layer of material was ablated from the target region (the resulting series of 2-dimensional elemental maps are presented in Figure S9, Supporting Information). Specimen stability to repeated rounds of XFM was assessed and found to introduce no measurable alterations in elemental content or distribution (see Supporting Information and Figure S10).

A portion of the target cell that contained both agglomerated NPs and non-NP Zn was selected for further analysis (white box, Figure 6A). The difference in elemental content, observed using XFM, before and after allowed the distribution of elements within the defined layers to be calculated (Figure 6B). In effect, these data enabled tracking the degree to which NPs penetrated into the cell. Surprisingly as NPs penetrated further into the cell the Zn:Co molar ratio continued to change (Figure 6C,D). After 5 cycles of XFM FIB-SEM had removed the micrometer of cellular material closest to the plasma membrane, the process was stopped as nearly all of the Zn and Co containing material within the NP agglomerate had been removed. The Zn:Co molar ratio of these most deeply internalized NPs, having penetrated further than 1 μm into the cell, had decreased to 6:1. This represented a 7-fold enrichment of Co within this agglomerated material and showed that particle dissolution continues unabated as these NPs move into the cell (Figure 6C,D).

The accumulation of NPs being limited to the first micrometer of cytoplasm (~30% of the cell's volume) is consistent with reports that particle internalization occurs *via* dynamin II-dependent endocytosis.[78] These early endosomal vesicles are rapidly acidified before delivering their contents to the lower pH environment of the lysosome,[79,80] where the acidic conditions typically encourage rapid dissolution of ZnO NPs.[6,37,81] Hence, the limited penetration of the NPs within the cell that was observed in this study may reflect their rapid dissolution; Table 2 provides evidence that the type of low pH environments encountered within cells are able to completely dissolve both Co-doped and undoped ZnO NPs within 24 h.

CONCLUSION

We have provided direct characterization of cellular NP-load across a population of human THP-1 monocyte-derived macrophages and demonstrated that these nanostructured materials undergo cell-mediated physiochemical modification after internalization. Quantification of NP uptake, as described here, allowed the number of NPs associated with a single cell to be assessed within the context of a representative cohort. This procedure was used to identify individual cells for more detailed analysis using high-resolution or iterative XFM FIB-SEM, a promising approach capable of providing insight into the 3-dimensional distribution and composition of metal oxide NPs postinternalization.

The current study supports the hypothesis that cell-mediated dissolution of NPs elevates total cellular Zn load, independent of localized NP agglomerates. For this family of nanomaterials, the idea of particle dissolution playing a causative role in disrupting cell function has been previously suggested,[1,4,16,37,60] but until recently unambiguous, direct evidence for cell-mediated NP dissolution has been lacking. The results presented here build on previous findings describing particle dissolution under physiological conditions,[59,70] and for the first time directly show that macrophages can alter NP composition. Although accurately determining changes to endogenous Zn levels postexposure to ZnO NPs remains a nontrivial exercise, the incorporation of a dopant into the particle structure provided a basis from which the formation of large intracellular NP agglomerates and internalization-dependent NP modification could be studied. These data suggest that the cell-mediated breakdown of internalized NPs is congruent with a damaging elevation in cellular Zn load, an interpretation supported by the recent identification of elevated intracellular Zn being strongly correlated with cytotoxicity.[77]

Accumulation of Zn with cells can be deleterious, despite being an essential inorganic cofactor for many cellular processes, including DNA synthesis, translation and transcription.[82,83] Recent work has provided evidence that Zn from exogenously applied metal oxide NPs interacts with the cell's set of native metalophilic ligands.[15] This finding complements the current work, indeed it is likely that liberation of Zn from NPs will overcome the cell's metal-ion buffering capacity, displacing endogenous metal ion cofactors and ultimately impair cell function.

By relating quantitative biochemical information regarding intracellular chemical processes (NP dissolution) to cellular ultrastructure (distance from the plasma membrane), the correlative photon and ion beam imaging techniques described here have provided significant insight into the biology of metal oxide nanoparticles at the cellular level. Although the primary focus here was the interactions between ZnO NPs and a prototypical *in vitro* model of human macrophages, the methodologies and approach we have described promise ready application to more general investigations of problems at the interface of material science and biology.

MATERIALS AND METHODS

Reagents. The Co-doped and undoped ZnO nanomaterials used in this study were made available through Micronisers (Australia) using their commercial processes. Unless otherwise stated all other reagents were analytical grade or higher and purchased from Sigma-Aldrich (St. Louis, MO, USA). Milli-Q ultraclean (resistivity >18 MΩ) water was used throughout this study.

Specimen Preparation. Human monocytes (THP-1 cell line) were seeded at 5×10^5 cells mL^{-1} in RPMI-1640 media (+ 10% FBS) onto 24 well plates containing silicon windows (window area 2 mm^2, membrane thickness 500 nm). The cells were differentiated into macrophages with the addition of phorbol myristate acetate at 20 nM overnight, after which nonadherent cells were removed. Adherent macrophages were then incubated for 24 h either with or without 40 nm ZnO nanoparticles, doped with 1.8% (w/w) Co, at 20 μg mL^{-1} or 15 μg mL^{-1} of $ZnCl_2$; in both cases these treatments induced 50% cytotoxicity. For imaging the THP-1 cells were removed from culture media, rinsed in fresh phosphate buffered saline, and immediately fixed for 2 h in 2.5% glutaraldehyde in 0.1 M sodium cacodylate containing 2 mM $CaCl_2$, pH 7.3−7.4 (adjusted with HCl). Cells were subsequently washed in 2 mM $CaCl_2$ and 0.1 M sodium cacodylate in distilled water for 10 min. Postfixation was carried out for 20 min in 1:1 osmium tetroxide (1% w/v) in 0.1 M sodium cacodylate with 2 mM $CaCl_2$. The cells were then washed in 0.1 M sodium cacodylate in 2 mM $CaCl_2$ in distilled water for 10 min to remove excess osmium tetroxide and then air-dried in a fume hood. Cobalt has previously been shown to substitute isomorphously for the zinc ions in the ZnO wurtzite lattice by use of channelling-enhanced microanalysis of the X-ray emission spectra from individual nanoparticles.[38]

Dissolution of ZnO Nanoparticles. The concentrations of Zn dissolved from nanoparticles were characterized *via* inductively coupled plasma (ICP) time of flight (TOF) mass spectrometry (MS). Nanoparticle solutions were incubated in cell culture media (with or without fetal bovine serum), water, or artificial lysosomal fluid for 24 h at 37 °C.[84] Solutions were then centrifuged through 3 kDa membrane filters (Microcon YM-3 filter, Millipore, USA) at 13500*g* for 60 min. Each solution was then diluted with ~3 vol % DD nitric acid in ultrapure (Milli-Q) water (15 mL). For drift correction, the internal standard In was added to each solution (at 30 ppb, diluted from a commercial stock solution). Solutions were then measured with a GBC Optimass 9500 ICP-TOF-MS instrument. Commercial stock solutions of Zn and Co were used for calibration standards (~10, 30, 70, and 100 ppb). All standards were ionic-strength adjusted, so as to contain the same high concentration of nitric acid present in the samples.

Powder Diffraction. Powder diffraction data were collected at the powder diffraction beamline at the Australian Synchrotron using a wavelength of 0.6888 Å on a 1.8 wt % doped CoO in ZnO powder sample packed in a 0.3 mm borosilicate glass capillary at ambient temperature. The wavelength was determined from a Rietveld refinement of a diluted LaB6 standard reference material (NIST, SRM 660b). The sample and the SRM were rotated during the data collection to maximize the powder average. In addition to the main phase, trace levels of hydrozincite (the starting material) and CoO (Figure S1, Supporting Information) were also observed. Reports by others that did not observe CoO at these low levels[40] used Cu Kα radiation from lab source, which will induce Co fluorescence reducing detection limits significantly.

X-ray Fluorescence Microscopy. The distribution of elements was mapped at the XFM beamline at the Australian Synchrotron.[85] An incident beam of either 10.0 or 12.7 keV X-rays (high-resolution and high-definition scans, respectively) was chosen to induce K-shell ionization of elements with atomic numbers below 30 ($Z \leq$ Zn), while also separating the scatter peaks from the fluorescence of lighter elements.

High-Resolution Elemental Mapping. The areal distribution of each element was determined using the Fresnel zone-plate microscope at the Australian Synchrotron XFM beamline. Because of the finite source size and beamline optics, the zone-plate illumination is not completely coherent, and a Ni knife-edge scan was used to determine the size of the focus to be 350 nm in the horizontal (*x*) and 250 nm in the vertical (*y*). The specimen was oriented at 90° to the incoming X-ray beam and scanned through the focal plane in steps of 300 nm (horizontal axis, *x*) and 200 nm (vertical axis, *y*) orthogonal to the beam axis using an integration of 2.5 s per scan point to ensure adequate counting statistics. A silicon-drift diode detector (Vortex, SII NanoTechnology, CA) oriented at 75° to the incident beam was used to detect the entire X-ray fluorescence spectrum at each pixel. Elemental maps were generated from the 3-dimensional data sets (*x*, *y*, energy) using the MAPS software suite (v1.6.5),[86] by fitting the recorded spectrum at every scan point to determine the fluorescence signal for each element. The procedure fitted the contribution of the K emission lines of Si, P, S, Cl, Ar, K, Ca, Ti, Cr, Mn, Fe, Co, Ni, Cu, and Zn as well as the Os L lines, where appropriate. The absolute calibration to areal densities (μg cm^{-2}) was adjusted by fitting the fluorescence signal from thin-film standards SRM-1832 and SRM-18323 (National Institute of Standards and Technology, Gaithersburg, MD, USA). The boundary of the cell under investigation was defined using the 2-dimensional projection map of X-ray scatter; P, S, and Ca were also useful, as these elements were found extensively throughout the target cell. For alignment of sequential scans, the original 2-dimensional maps were first cropped to contain the region of interest (non-FIBed region), and then aligned using cross correlation to find the optimal offsets in *x* and *y* axis. These values were then applied to the entire 2-dimensional map; in almost all cases the resulting offsets were minimal (unidirectional single pixel movements). To obtain the elemental "difference maps" (Δ_x), which showed the distribution of elements through the ablated region, a median filter (radius 1) was applied to each image pair before subtraction.

High-Definition Elemental Mapping. The incident beam was focused to a spot ~2 μm (full-width at half-maximum, fwhm) using a Kirkpatrick−Baez mirror pair. The specimen was continuously scanned through the focus using a step size of 2 μm, well-matched to the dimensions of the beam spot. Full XRF spectral images were obtained at each pixel with an effective dwell time of ~15 ms meaning high definition scans were collected in under 2 h. The low-latency, large solid angle 384-channel Maia XRF detector was positioned in the backscatter geometry, and the resulting elemental maps ranged up to 400 000 pixels in size. During these experiments single element foils, Mn and Pt (Micromatter, Canada), were scanned in the same geometry and used as references to establish elemental quantitation. Deconvolution of the Maia data was performed using the GeoPIXE v6.4w (CSIRO, Australia) that incorporates a linear transformation matrix to perform spectral deconvolution.[87] Spectra were calibrated using the metal foil measurements, and corrections made for self-absorption in the sample, absorption in air, and the efficiency response of the detector.[88] The detected X-ray photons from each pixel were related to calculated-model fluorescence X-ray yields for an assumed specimen composition

and thickness. The composition and thickness of the silicon nitride window were known from the manufacturers, and the composition and average density typical of dried organic material ($C_{22}H_{10}N_2O_4$ and 1.42 g cm^{-3}, respectively)[89] was used to model the bulk cell, while the density of NPs was assumed to be 5.61 g cm^{-3} with a composition as described above. Absorption effects for XRF from the lowest atomic number element relevant to this study (Ca Kα radiation for the Maia) are negligible for this specimen type.

Focused Ion Beam Ablation. Focused ion beam (FIB) milling was performed with a FEI Nanolab Helios 600 (FEI Company, OR, USA) equipped with a field emission gun. A liquid metal ion source (LMIS) of Ga^+ was employed, with the accelerating voltage set to 30 kV. During milling, ion current was set to 48 pA, and the corresponding beam diameter was approximately 20 nm fwhm. In order to obtain uniform ion dose on the target cell, fast scanning was preferred with dwell time set at 100 ns pixel^{-1}. Electron beam imaging was for feature location and alignment only, and the dose was limited to as low as achievable so as to minimize the potential for damaging the sample.

Image Analysis. Image analysis of elemental maps was performed using a combination of tools native to GeoPIXE, MAPS, and ImageJ v1.46j, a java-based image processing program developed by the National Institutes of Health (USA).[90,91]

Intensity Correlation Analysis. Correlation of element intensity between scans was quantitatively analyzed using described methods.[50] In brief, we calculated the function $(A_i - a)(B_i - b)$, where i represents pixel number, A and B are the normalized pixel intensities for the first (A) and second scans (B) and a and b are their respective means. Distributions that skew to the right reflect dependent localization (where the two pixel elemental content values vary synchronously); ones that are symmetrical about $x = 0$ indicate no association between the two images (random), while those that skew to the left reflect independent localization, where pixel intensity varies inversely (anticorrelated). Reciprocal analysis was performed by alternating the designated first and second signals and identified no dependence on order. The intensity correlation quotient (ICQ) reflects the ratio of the number of positive $(A_i - a)(B_i - b)$ values to the total number of pixels in the region of interest (ROI) corrected to a range of −0.5 (independent staining) to +0.5 (dependent staining) by subtracting 0.5.[92]

Cluster Analysis. Two-dimensional elemental maps were segmented using the *k*-means clustering algorithm incorporated in the statistics package JMP (SAS Institute Inc., NC, USA). For a single 2-dimensional map, the intensities at each pixel are considered as a 1-dimensional population, resulting from a mixture of populations from multiple origins. For the Zn maps, pixel intensities were grouped into one of three populations' background, non-NP Zn and NP Zn.

Identifying Cells. Using high definition XFM scans to quantitate elemental content on a per cell basis required a mask of each cell position to be constructed. This was derived from the product of elastic and inelastic scatter normalized to the abundance of Ca at each pixel, the resulting signal associated with cells was approximately uniform and readily able to differentiate cells from noncell structures. Finally the quality of the mask was assessed by coregistering this binary image with an optical micrograph of the same field of cells (Figure S2, Supporting Information).

In the case of quantitating the Zn:Co molar ratio of cell-associated NP agglomerates, the same mask was used but with an additional step where it was combined using ImageJ's in built AND function with the elemental map of Co distribution. In this way NPs colocalized with cells could be included/excluded from the analysis as appropriate.

Assessing NP Internalization Depth. To avoid artifacts arising from the edges of a scan, a region of interest (ROI), approximately 9 μm by 23 μm, was selected for further processing. This ROI consisted of subregions containing both NP and non-NP Zn (shown in red and green, respectively, Figure S5, Supporting Information). For visualization, NP penetration into the cell the XRF map for each element was subtracted from the preceding image in consecutive cycles. Such "differential" maps reflected the distribution of elements within the layer ablated during FIB milling. As the layer thickness in this study was comparable to the lateral pixel size in each XFM map, a 3-dimensional reconstruction could be achieved, using the cell membrane as the original reference surface, an approach particularly informative for adherent cells.

Atomic Force Microscopy. Atomic Force Microscopy was performed on Dimension Icon SPM System (Veeco Instruments Inc., NY, USA) to provide surface measurement with submicrometer accuracy. The milling profile of the cells was measured using tapping mode, and the AFM images were visualized and analyzed NanoScope Analysis (software supplied by the manufacturer). Milling depth a single dose achieved was estimated by averaging the surface height change between milled and nonmilled regions (5 independent profiles).

Statistical Analysis. Where appropriate, differences in group means were assessed using Student's *t* test using Welch's correction for unequal variances.[58] When comparisons were made across more than two groups, a one-way ANOVA using Bonferroni's multiple comparison *posthoc* test was used. Data transformations, significance tests, and curve fitting were performed using either JMP or Graphpad Prism v5.0. Nonlinear curve fitting utilized the Levenberg−Marquardt method. Comparisons between the goodness of fit for nested models, *i.e.*, Gaussian ($X \sim N_{(\mu,\sigma^2)}$) *vs* a sum of Gaussians ($X' = \sum_{i=1}^{n} X_i$) with respect to measured data were assessed using the Akaike information criterion and the exact sum of squares *F*-test.[24,93] Deviation of experimental data from the model was assessed using Wald−Wolfowitz runs test and D'Agostino's omnibus K^2. Throughout this work the significance level is defined as $p < 0.05$.

Conflict of Interest: The authors declare the following competing financial interest(s): The authors report no conflicts of interest, except for TWT who is chief technical officer of Micronisers Australasia Pty Ltd, a manufacturer of ZnO NPs. The authors alone are responsible for the content and writing of the paper.

Acknowledgment. The authors would like to thank Yi Chen, Douglas Mair, Joan Clark and Zoran Vasic for their technical assistance during the experiments and acknowledge support from the Australian Synchrotron and CSIRO OCE Postdoctoral Fellowship Programs (S.A.J.) and the New Staff Member Research Fund of Monash University (J.F.). Parts of this research were undertaken on the XFM beamline at the Australian Synchrotron, at the Melbourne Centre for Nanofabrication (MCN) in the Victorian Node of the Australian National Fabrication Facility (ANFF) and the Monash Centre for Electron Microscopy. This work has been supported in part by the Advanced Manufacturing Cooperative Research Centre (AMCRC) and the National Health and Medical Research Council (NHMRC) Project Grant #616621.

Supporting Information Available: Additional figures and discussion material as described in the text is available free of charge *via* the Internet at http://pubs.acs.org.

REFERENCES AND NOTES

1. Nel, A. E.; Madler, L.; Velegol, D.; Xia, T.; Hoek, E. M. V.; Somasundaran, P.; Klaessig, F.; Castranova, V.; Thompson, M. Understanding Biophysicochemical Interactions at the Nano-Bio Interface. *Nat. Mater.* **2009**, *8*, 543–557.
2. Ma, H.; Williams, P. L.; Diamond, S. A. Ecotoxicity of Manufactured ZnO Nanoparticles—A Review. *Environ. Pollut.* **2013**, *172*, 76–85.
3. Nel, A.; Xia, T.; Mädler, L.; Li, N. Toxic Potential of Materials at the Nanolevel. *Science* **2006**, *311*, 622–627.
4. Song, W.; Zhang, J.; Guo, J.; Zhang, J.; Ding, F.; Li, L.; Sun, Z. Role of the Dissolved Zinc Ion and Reactive Oxygen Species in Cytotoxicity of ZnO Nanoparticles. *Toxicol. Lett.* **2010**, *199*, 389–397.
5. Kim, Y. H.; Fazlollahi, F.; Kennedy, I. M.; Yacobi, N. R.; Hamm-Alvarez, S. F.; Borok, Z.; Kim, K.-J.; Crandall, E. D. Alveolar Epithelial Cell Injury Due to Zinc Oxide Nanoparticle Exposure. *Am. J. Respir. Crit. Care Med.* **2010**, *182*, 1398–1409.
6. George, S.; Pokhrel, S.; Xia, T.; Gilbert, B.; Ji, Z.; Schowalter, M.; Rosenauer, A.; Damoiseaux, R.; Bradley, K. A.; Mädler, L.; *et al.* Use of a Rapid Cytotoxicity Screening Approach To Engineer a Safer Zinc Oxide Nanoparticle through Iron Doping. *ACS Nano* **2009**, *4*, 15–29.

7. Biancamaria, B.; Maria Grazia, E.; Felice, L.; Michela, I.; Raimondo, P.; Lopez-Quintela, A. M. Penetration of Metallic Nanoparticles in Human Full-Thickness Skin. *J. Invest. Dermatol.* **2007**, *127*, 1701–1712.
8. Monteiro-Riviere, N. A.; Wiench, K.; Landsiedel, R.; Schulte, S.; Inman, A. O.; Riviere, J. E. Safety Evaluation of Sunscreen Formulations Containing Titanium Dioxide and Zinc Oxide Nanoparticles in UVB Sunburned Skin: An *In Vitro* and *In Vivo* Study. *Toxicol. Sci.* **2011**, *123*, 264–280.
9. Gulson, B.; McCall, M.; Korsch, M.; Gomez, L.; Casey, P.; Oytam, Y.; Taylor, A.; McCulloch, M.; Trotter, J.; Kinsley, L.; *et al.* Small Amounts of Zinc from Zinc Oxide Particles in Sunscreens Applied Outdoors Are Absorbed through Human Skin. *Toxicol. Sci.* **2010**, *118*, 140–149.
10. Mosser, D. M.; Edwards, J. P. Exploring the Full Spectrum of Macrophage Activation. *Nat. Rev. Immunol.* **2008**, *8*, 958–969.
11. Feltis, B. N.; O'Keefe, S. J.; Harford, A. J.; Piva, T. J.; Turney, T. W.; Wright, P. F. A. Independent Cytotoxic and Inflammatory Responses to Zinc Oxide Nanoparticles in Human Monocytes and Macrophages. *Nanotoxicology* **2012**, *6*, 757–765.
12. Roy, R.; Tripathi, A.; Das, M.; Dwivedi, P. D. Cytotoxicity and Uptake of Zinc Oxide Nanoparticles Leading to Enhanced Inflammatory Cytokines Levels in Murine Macrophages: Comparison with Bulk Zinc Oxide. *J. Biomed. Nanotechnol.* **2011**, *7*, 110–111.
13. Sharma, V.; Anderson, D.; Dhawan, A. Zinc Oxide Nanoparticles Induce Oxidative DNA Damage and ROS-Triggered Mitochondria Mediated Apoptosis in Human Liver Cells (HepG2). *Apoptosis* **2012**, *17*, 852–870.
14. Javed Akhtar, M.; Ahamed, M.; Sudhir, K.; Majeed Khan, M. A.; Ahmad, J.; Alrokayan, S. A. Zinc Oxide Nanoparticles Selectively Induce Apoptosis in Human Cancer Cells Through Reactive Oxygen Species. *Int. J. Nanomed.* **2012**, *7*, 845–857.
15. Gilbert, B.; Fakra, S. C.; Xia, T.; Pokhrel, S.; Mädler, L.; Nel, A. E. The Fate of ZnO Nanoparticles Administered to Human Bronchial Epithelial Cells. *ACS Nano* **2012**, *6*, 4921–4930.
16. Xia, T.; Kovochich, M.; Liong, M.; Mädler, L.; Gilbert, B.; Shi, H.; Yeh, J. I.; Zink, J. I.; Nel, A. E. Comparison of the Mechanism of Toxicity of Zinc Oxide and Cerium Oxide Nanoparticles Based on Dissolution and Oxidative Stress Properties. *ACS Nano* **2008**, *2*, 2121–2134.
17. Moos, P. J.; Chung, K.; Woessner, D.; Honeggar, M.; Cutler, N. S.; Veranth, J. M. ZnO Particulate Matter Requires Cell Contact for Toxicity in Human Colon Cancer Cells. *Chem. Res. Toxicol.* **2010**, *23*, 733–739.
18. Mudunkotuwa, I. A.; Rupasinghe, T.; Wu, C.-M.; Grassian, V. H. Dissolution of ZnO Nanoparticles at Circumneutral pH: A Study of Size Effects in the Presence and Absence of Citric Acid. *Langmuir* **2011**, *28*, 396–403.
19. Turney, T. W.; Duriska, M. B.; Jayaratne, V.; Elbaz, A.; O'Keefe, S. J.; Hastings, A. S.; Piva, T. J.; Wright, P. F. A.; Feltis, B. N. Formation of Zinc-Containing Nanoparticles from Zn^{2+} Ions in Cell Culture Media: Implications for the Nanotoxicology of ZnO. *Chem. Res. Toxicol.* **2012**, *25*, 2057–2066.
20. Yi, Y.-Z.; Jiang, S.-J.; Sahayam, A. C. Palladium Nanoparticles as the Modifier for the Determination of Zn, As, Cd, Sb, Hg and Pb in Biological Samples by Ultrasonic Slurry Sampling Electrothermal Vaporization Inductively Coupled Plasma Mass Spectrometry. *J. Anal. At. Spectrom.* **2012**, *27*, 426–431.
21. Chaurand, P. Imaging Mass Spectrometry of Thin Tissue Sections: A Decade of Collective Efforts. *J. Proteomics* **2012**, *75*, 4883–4892.
22. Drescher, D.; Giesen, C.; Traub, H.; Panne, U.; Kneipp, J.; Jakubowski, N. Quantitative Imaging of Gold and Silver Nanoparticles in Single Eukaryotic Cells by Laser Ablation ICP-MS. *Anal. Chem.* **2012**, *84*, 9684–9688.
23. Zheng, J.; Nagashima, K.; Parmiter, D.; Cruz, J.; Patri, A. SEM X-ray Microanalysis of Nanoparticles Present in Tissue or Cultured Cell Thin Sections. In *Characterization of Nanoparticles Intended for Drug Delivery*; McNeil, S. E., Ed.; Humana Press: New York, 2011; Vol. 697, pp 93–99.
24. Aronova, M. A.; Kim, Y. C.; Harmon, R.; Sousa, A. A.; Zhang, G.; Leapman, R. D. Three-Dimensional Elemental Mapping of Phosphorus by Quantitative Electron Spectroscopic Tomography (QuEST). *J. Struct. Biol.* **2007**, *160*, 35–48.
25. Rigort, A.; Bäuerlein, F. J. B.; Villa, E.; Eibauer, M.; Laugks, T.; Baumeister, W.; Plitzko, J. M. Focused Ion Beam Micromachining of Eukaryotic Cells for Cryoelectron Tomography. *Proc. Natl. Acad. Sci. U. S. A.* **2012**, *109*, 4449–4454.
26. Hitchcock, A. P.; Dynes, J. J.; Johansson, G.; Wang, J.; Botton, G. Comparison of NEXAFS Microscopy and TEM-EELS for Studies of Soft Matter. *Micron* **2008**, *39*, 311–319.
27. Plascencia-Villa, G.; Starr, C. R.; Armstrong, L. S.; Ponce, A.; Jose-Yacaman, M. Imaging Interactions of Metal Oxide Nanoparticles with Macrophage Cells by Ultra-High Resolution Scanning Electron Microscopy Techniques. *Integr. Biol.* **2012**, *4*, 1358–1366.
28. Dean, K. M.; Qin, Y.; Palmer, A. E. Visualizing Metal Ions in Cells: An Overview of Analytical Techniques, Approaches, and Probes. *Biochim. Biophys. Acta, Mol. Cell Res.* **2012**, *1823*, 1406–1415.
29. Klar, T. A.; Feldmann, J. Fluorophore–Metal Nanoparticle Interactions and Their Applications in Biosensing. In *Complex-Shaped Metal Nanoparticles*; Wiley-VCH Verlag GmbH & Co. KGaA: Weinheim, 2012; pp 395–427.
30. Price, K. A.; Hickey, J. L.; Xiao, Z.; Wedd, A. G.; James, S. A.; Liddell, J. R.; Crouch, P. J.; White, A. R.; Donnelly, P. S. The Challenges of Using a Copper Fluorescent Sensor (CS1) to Track Intracellular Distributions of Copper in Neuronal and Glial Cells. *Chem. Sci.* **2012**, *3*, 2748–2759.
31. Wolford, J. L.; Chishti, Y.; Jin, Q.; Ward, J.; Chen, L.; Vogt, S.; Finney, L. Loss of Pluripotency in Human Embryonic Stem Cells Directly Correlates with an Increase in Nuclear Zinc. *PLoS One* **2010**, *5*, e12308.
32. Chen, H.-H.; Chien, C.-C.; Petibois, C.; Wang, C.-L.; Chu, Y. S.; Lai, S.-F.; Hua, T.-E.; Chen, Y.-Y.; Cai, X.; Kempson, I. M.; *et al.* Quantitative Analysis of Nanoparticle Internalization in Mammalian Cells by High Resolution X-ray Microscopy. *J. Nanobiotechnol.* **2011**, *9*, 14.
33. McRae, R.; Lai, B.; Vogt, S.; Fahrni, C. J. Correlative μXRF and Optical Immunofluorescence Microscopy of Adherent Cells Labeled with Ultrasmall Gold Particles. *J. Struct. Biol.* **2006**, *155*, 22–29.
34. Astolfo, A.; Arfelli, F.; Schultke, E.; James, S. A.; Mancini, L.; Menk, R.-H. A Detailed Study of Gold-Nanoparticle Loaded Cells Using X-ray Based Techniques for cell-Tracking Applications with Single-Cell Sensitivity. *Nanoscale* **2013**, *5*, 3337–3345.
35. McColl, G.; James, S. A.; Mayo, S.; Howard, D. L.; Ryan, C. G.; Kirkham, R.; Moorhead, G. F.; Paterson, D.; de Jonge, M. D.; Bush, A. I. *Caenorhabditis elegans* Maintains Highly Compartmentalized Cellular Distribution of Metals and Steep Concentration Gradients of Manganese. *PLoS One* **2012**, *7*, e32685.
36. Vogt, S.; Lanzirotti, A. Trends in X-ray Fluorescence Microscopy. *Synchrotron Radiat. News* **2013**, *26*, 32–38.
37. Xia, T.; Zhao, Y.; Sager, T.; George, S.; Pokhrel, S.; Li, N.; Schoenfeld, D.; Meng, H.; Lin, S.; Wang, X.; *et al.* Decreased Dissolution of ZnO by Iron Doping Yields Nanoparticles with Reduced Toxicity in the Rodent Lung and Zebrafish Embryos. *ACS Nano* **2011**, *5*, 1223–1235.
38. Casey, P. S.; Rossouw, C. J.; Boskovic, S.; Lawrence, K. A.; Turney, T. W. Incorporation of Dopants into the Lattice of ZnO Nanoparticles to Control Photoactivity. *Superlattices Microstruct.* **2006**, *39*, 97–106.
39. He, R.; Hocking, R. K.; Tsuzuki, T. Co-Doped ZnO Nanopowders: Location of Cobalt and Reduction in Photocatalytic Activity. *Mater. Chem. Phys.* **2012**, *132*, 1035–1040.
40. Hays, J.; Reddy, K. M.; Graces, N. Y.; Engelhard, M. H.; Shutthanandan, V.; Luo, M.; Xu, C.; Giles, N. C.; Wang, C.; Thevuthasan, S.; *et al.* Effect of Co Doping on the Structural, Optical and Magnetic Properties of ZnO Nanoparticles. *J. Phys: Condens. Matter* **2007**, *19*, 266203.
41. Schulze, C.; Kroll, A.; Lehr, C.-M.; Schäfer, U. F.; Becker, K.; Schnekenburger, J.; Landsiedel, R.; Wohlleben, W. Not Ready to Use—Overcoming Pitfalls when Dispersing Nanoparticles in Physiological Media. *Nanotoxicology* **2008**, *2*, 51–61.

42. Maiorano, G.; Sabella, S.; Sorce, B.; Brunetti, V.; Malvindi, M. A.; Cingolani, R.; Pompa, P. P. Effects of Cell Culture Media on the Dynamic Formation of Protein−Nanoparticle Complexes and Influence on the Cellular Response. *ACS Nano* **2010**, *4*, 7481–7491.
43. Sabuncu, A. C.; Grubbs, J.; Qian, S.; Abdel-Fattah, T. M.; Stacey, M. W.; Beskok, A. Probing Nanoparticle Interactions in Cell Culture Media. *Colloids Surf., B* **2012**, *95*, 96–102.
44. Merkus, H. G. *Particle Size Measurements*; Springer: Berlin, 2009; Vol. 17.
45. Matsuyama, S.; Shimura, M.; Fujii, M.; Maeshima, K.; Yumoto, H.; Mimura, H.; Sano, Y.; Yabashi, M.; Nishino, Y.; Tamasaku, K.; *et al.* Elemental Mapping of Frozen-Hydrated Cells with Cryo-Scanning X-ray Fluorescence Microscopy. *X-ray Spectrom.* **2010**, *39*, 260–266.
46. Hayat, A. *Principles and Techniques of Electron Microscopy: Biological Applications*; Cambridge University Press: Cambridge, U.K., 2000.
47. Francis, L. W.; Gonzalez, D.; Ryder, T.; Baer, K.; Rees, M.; White, J. O.; Conlan, R. S.; Wright, C. J. Optimized Sample Preparation for High-Resolution AFM Characterization of Fixed Human Cells. *J. Microsc.* **2010**, *240*, 111–121.
48. Hernandez-Viezcas, J. A.; Castillo-Michel, H.; Andrews, J. C.; Cotte, M.; Rico, C.; Peralta-Videa, J. R.; Ge, Y.; Priester, J. H.; Holden, P. A.; Gardea-Torresdey, J. L. *In Situ* Synchrotron X-ray Fluorescence Mapping and Speciation of CeO_2 and ZnO Nanoparticles in Soil Cultivated Soybean (*Glycine max*). *ACS Nano* **2013**, *7*, 1415–1423.
49. Voet, D.; Voet, J. *Biochemistry*; John Wiley & Sons: New York, 1995.
50. Li, Q.; Lau, A.; Morris, T. J.; Guo, L.; Fordyce, C. B.; Stanley, E. F. A Syntaxin 1, Gαo, and N-Type Calcium Channel Complex at a Presynaptic Nerve Terminal: Analysis by Quantitative Immunocolocalization. *J. Neurosci.* **2004**, *24*, 4070–4081.
51. Ryan, C. G.; Siddons, D. P.; Kirkham, R.; Dunn, P. A.; Kuczewski, A. J.; Moorhead, G.; De Geronimo, G.; Paterson, D. J.; de Jonge, M. D.; Hough, R. M.; *et al.* The New Maia Detector System: Methods For High Definition Trace Element Imaging Of Natural Material. *AIP Conf. Proc.* **2010**, *1234*, 240–243.
52. James, S. A.; de Jonge, M. D.; Howard, D. L.; Bush, A. I.; Paterson, D.; McColl, G. Direct *In Vivo* Imaging of Essential Bioinorganics in *Caenorhabditis elegans*. *Metallomics* **2013**, *5*, 627–635.
53. Limpert, E.; Stahel, W. A.; Abbt, M. Log-Normal Distributions Across the Sciences: Keys and Clues. *BioScience* **2001**, *51*, 341–352.
54. Furusawa, C.; Suzuki, T.; Kashiwagi, A.; Yomo, T.; Kaneko, K. Ubiquity of Log-Normal Distributions in Intra-Cellular Reaction Dynamics. *Biophysics* **2005**, *1*, 25–31.
55. Strom, T. S.; Anur, P.; Prislovsky, A. A Numerical Analysis Model for Interpretation of Flow Cytometric Studies of *Ex Vivo* Phagocytosis. *PLoS One* **2011**, *6*, e26657.
56. Rempala, G.; Wesolowski, J.; Politechnika, W. Asymptotics for Products of Sums and U-Statistics. *Electron. Commun. Probab.* **2002**, *7*, 47–54.
57. Maheshri, N.; O'Shea, E. K. Living with Noisy Genes: How Cells Function Reliably with Inherent Variability in Gene Expression. *Annu. Rev. Biophys. Biomol. Struct.* **2007**, *36*, 413–434.
58. Irving, H.; Williams, R. J. P. The Stability of Transition-Metal Complexes. *J. Chem. Soc.* **1953**, *0*, 3192–3210.
59. Müller, K., H.; Kulkarni, J.; Motskin, M.; Goode, A.; Winship, P.; Skepper, J. N.; Ryan, M. P.; Porter, A. E. pH-Dependent Toxicity of High Aspect Ratio ZnO Nanowires in Macrophages Due to Intracellular Dissolution. *ACS Nano* **2010**, *4*, 6767–6779.
60. Sasidharan, A.; Chandran, P.; Menon, D.; Raman, S.; Nair, S.; Koyakutty, M. Rapid Dissolution of ZnO Nanocrystals in Acidic Cancer Microenvironment Leading to Preferential Apoptosis. *Nanoscale* **2011**, *3*, 3657–3669.
61. Franklin, N. M.; Rogers, N. J.; Apte, S. C.; Batley, G. E.; Gadd, G. E.; Casey, P. S. Comparative Toxicity of Nanoparticulate ZnO, Bulk ZnO, and $ZnCl_2$ to a Freshwater Microalga (*Pseudokirchneriella subcapitata*): The Importance of Particle Solubility. *Environ. Sci. Technol.* **2007**, *41*, 8484–8490.
62. Mulet, J.; Llopis-Torregrosa, V.; Primo, C.; Marqués, M. C.; Yenush, L. Endocytic Regulation of Alkali Metal Transport Proteins in Mammals, Yeast and Plants. *Curr. Genet.* **2013**, 1–24.
63. Forbes, J. R.; Gros, P. Iron, Manganese, and Cobalt Transport by Nramp1 (Slc11a1) and Nramp2 (Slc11a2) Expressed at the Plasma Membrane. *Blood* **2003**, *102*, 1884–1892.
64. Howitt, J.; Putz, U.; Lackovic, J.; Doan, A.; Dorstyn, L.; Cheng, H.; Yang, B.; Chan-Ling, T.; Silke, J.; Kumar, S.; *et al.* Divalent Metal Transporter 1 (DMT1) Regulation by Ndfip1 Prevents Metal Toxicity in Human Neurons. *Proc. Natl. Acad. Sci. U. S. A.* **2009**, *106*, 15489–15494.
65. Nevo, Y.; Nelson, N. The NRAMP Family of Metal-Ion Transporters. *Biochim. Biophys. Acta, Mol. Cell Res.* **2006**, *1763*, 609–620.
66. Wagner, D.; Maser, J.; Moric, I.; Boechat, N.; Vogt, S.; Gicquel, B.; Lai, B.; Reyrat, J.-M.; Bermudez, L. Changes of the Phagosomal Elemental Concentrations by *Mycobacterium tuberculosis* Mramp. *Microbiology* **2005**, *151*, 323–332.
67. Haase, H.; Rink, L. Zinc Signals and Immune Function. *BioFactors* **2013**, 10.1002/biof.1114.
68. Zhou, J.; Xu, N. S.; Wang, Z. L. Dissolving Behavior and Stability of ZnO Wires in Biofluids: A Study on Biodegradability and Biocompatibility of ZnO Nanostructures. *Adv. Mater.* **2006**, *18*, 2432–2435.
69. Casey, J. R.; Grinstein, S.; Orlowski, J. Sensors and Regulators of Intracellular pH. *Nat. Rev. Mol. Cell Biol.* **2010**, *11*, 50–61.
70. Cho, W.-S.; Duffin, R.; Howie, S.; Scotton, C.; Wallace, W.; MacNee, W.; Bradley, M.; Megson, I.; Donaldson, K. Progressive Severe Lung Injury by Zinc Oxide Nanoparticles; the Role of Zn^{2+} Dissolution Inside Lysosomes. *Part. Fibre Toxicol.* **2011**, *8*, 27.
71. Cho, W.-S.; Duffin, R.; Poland, C. A.; Duschl, A.; Oostingh, G. J.; MacNee, W.; Bradley, M.; Megson, I. L.; Donaldson, K. Differential Pro-Inflammatory Effects of Metal Oxide Nanoparticles and their Soluble Ions *In Vitro* and *In Vivo*; Zinc and Copper Nanoparticles, But Not Their Ions, Recruit Eosinophils to the Lungs. *Nanotoxicology* **2012**, *6*, 22–35.
72. Hanley, C.; Thurber, A.; Hanna, C.; Punnoose, A.; Zhang, J.; Wingett, D. The Influences of Cell Type and ZnO Nanoparticle Size on Immune Cell Cytotoxicity and Cytokine Induction. *Nanoscale Res. Lett.* **2009**, *4*, 1409–1420.
73. Lin, W.; Xu, Y.; Huang, C.-C.; Ma, Y.; Shannon, K.; Chen, D.-R.; Huang, Y.-W. Toxicity of Nano- and Micro-Sized ZnO Particles in Human Lung Epithelial Cells. *J. Nanopart. Res.* **2009**, *11*, 25–39.
74. Chevion, M. A Site-Specific Mechanism for Free Radical Induced Biological Damage: The Essential Role of Redox-Active Transition Metals. *Free Radical Biol. Med.* **1988**, *5*, 27–37.
75. Krężel, A.; Hao, Q.; Maret, W. The Zinc/Thiolate Redox Biochemistry of Metallothionein and the Control of Zinc Ion Fluctuations in Cell Signaling. *Arch. Biochem. Biophys.* **2007**, *463*, 188–200.
76. Musatov, A.; Robinson, N. C. Susceptibility of Mitochondrial Electron-Transport Complexes to Oxidative Damage. Focus on Cytochrome C Oxidase. *Free Radical Res.* **2012**, *46*, 1313–1326.
77. Shen, C.; James, S. A.; de Jonge, M. D.; Turney, T. W.; Wright, P. F. A.; Feltis, B. N. Relating Cytotoxicity, Zinc Ions, and Reactive Oxygen in ZnO Nanoparticle-Exposed Human Immune Cells. *Toxicol. Sci.* **2013**, 10.1093/toxsci/kft187.
78. Lunov, O.; Syrovets, T.; Loos, C.; Beil, J.; Delacher, M.; Tron, K.; Nienhaus, G. U.; Musyanovych, A.; Mailänder, V.; Landfester, K.; *et al.* Differential Uptake of Functionalized Polystyrene Nanoparticles by Human Macrophages and a Monocytic Cell Line. *ACS Nano* **2011**, *5*, 1657–1669.
79. Benjaminsen, R. V.; Sun, H.; Henriksen, J. R.; Christensen, N. M.; Almdal, K.; Andresen, T. L. Evaluating Nanoparticle Sensor Design for Intracellular pH Measurements. *ACS Nano* **2011**, *5*, 5864–5873.
80. Tycko, B.; Keith, C. H.; Maxfield, F. R. Rapid Acidification of Endocytic Vesicles Containing Asialoglycoprotein in Cells of a Human Hepatoma Line. *J. Cell Biol.* **1983**, *97*, 1762–1776.

81. Wilhelmi, V.; Fischer, U.; Weighardt, H.; Schulze-Osthoff, K.; Nickel, C.; Stahlmecke, B.; Kuhlbusch, T. A. J.; Scherbart, A. M.; Esser, C.; Schins, R. P. F.; *et al.* Zinc Oxide Nanoparticles Induce Necrosis and Apoptosis in Macrophages in a p47phox- and Nrf2-Independent Manner. *PLoS One* **2013**, *8*, e65704.
82. Mato, S.; Sánchez-Gómez, M. V.; Bernal-Chico, A.; Matute, C. Cytosolic Zinc Accumulation Contributes to Excitotoxic Oligodendroglial Death. *Glia* **2013**, *61*, 750–764.
83. Blindauer, C. A.; Harrison, M. D.; Parkinson, J. A.; Robinson, A. K.; Cavet, J. S.; Robinson, N. J.; Sadler, P. J. A Metallothionein Containing a Zinc Finger Within a Four-Metal Cluster Protects a Bacterium from Zinc Toxicity. *Proc. Natl. Acad. Sci. U. S. A.* **2001**, *98*, 9593–9598.
84. Midander, K.; Wallinder, I. O.; Leygraf, C. *In Vitro* Studies of Copper Release from Powder Particles in Synthetic Biological Media. *Environ. Pollut.* **2007**, *145*, 51–59.
85. Paterson, D.; de Jonge, M. D.; Howard, D. L.; Lewis, W.; McKinlay, J.; Starritt, A.; Kusel, M.; Ryan, C. G.; Kirkham, R.; Moorhead, G.; *et al.* The X-ray Fluorescence Microscopy Beamline at the Australian Synchrotron. *AIP Conf. Proc.* **2011**, *1365*, 219–222.
86. Vogt, S. MAPS: A Set of Software Tools for Analysis and Visualization of 3D X-ray Fluorescence Data sets. *J. Phys. IV* **2003**, *104*, 635–638.
87. Ryan, C. G. Quantitative Trace Element Imaging Using PIXE and the Nuclear Microprobe. *Int. J. Imaging Syst. Technol.* **2000**, *11*, 219–230.
88. Ryan, C. G. Developments in Dynamic Analysis for Quantitative PIXE True Elemental Imaging. *Nucl. Instrum. Methods Phys. Res., Sect. B* **2001**, *181*, 170–179.
89. McMaster, W. H.; Kerr del Grande, N.; Mallett, J. H.; Hubbell, J. H. Compilation of X-ray Cross Sections, UCRL-50174 Section II Revision I. *National Technical Information Services L-3*; U.S. Department of Commerce: Washington, D.C., 1969.
90. Kocsis, E.; Trus, B. L.; Steer, C. J.; Bisher, M. E.; Steven, A. C. Image Averaging of Flexible Fibrous Macromolecules: The Clathrin Triskelion has an Elastic Proximal Segment. *J. Struct. Biol.* **1991**, *107*, 6–14.
91. Schneider, C. A.; Rasband, W. S.; Eliceiri, K. W. NIH Image to ImageJ: 25 Years of Image Analysis. *Nat. Methods* **2012**, *9*, 671–675.
92. Bolte, S.; Cordelieres, F. P. A Guided Tour into Subcellular Colocalization Analysis in Light Microscopy. *J. Microsc.* **2006**, *224*, 213–232.
93. Brown, A. M. A Step-By-Step guide to Non-Linear Regression Analysis of Experimental Data Using a Microsoft Excel Spreadsheet. *Comput. Methods Programs Biomed.* **2001**, *65*, 191–200.